Published in final edited form as:
Nat Nanotechnol. 2016 December ; 11(12): 1112–1119. doi:10.1038/nnano.2016.150.

Quantum dot-loaded monofunctionalized DNA Icosahedra for single particle tracking of endocytic pathways

Dhiraj Bhatia[1,2], **Senthil Arumugam**[1], **Michel Nasilowski**[3], **Himanshu Joshi**[4], **Christian Wunder**[1], **Valerie Chambon**[1], **Ved Prakash**[2,5], **Chloé Grazon**[6], **Brice Nadal**[6], **Prabal K. Maiti**[4], **Ludger Johannes**[1,7], **Benoit Dubertret**[3,7], and **Yamuna Krishnan**[2,5,7,8]

[1]Institut Curie, PSL Research University, Chemical Biology of Membranes and Therapeutic Delivery unit, INSERM, U 1143, CNRS, UMR 3666, 26 rue d'Ulm, 75248 Paris Cedex 05, France

[2]National Centre for Biological Sciences, Tata Institute of Fundamental Research, GKVK, Bellary Road, Bangalore 560065, India

[3]Laboratoire Physique et Etude des Matériaux UMR8213 ESPCI ParisTech–CNRS - UPMC Sorbonne Universités 10 rue Vauquelin, 75005 Paris, France

[4]Center for condensed matter theory, Department of Physics, Indian Institute of Science, Bangalore 560012

[5]Department of Chemistry, The University of Chicago, 929 E, 57th St., Chicago, IL 60637, USA

[6]Nexdot, 10 rue Vauquelin, 75005 Paris, France

[7]Grossman Institute for Neuroscience, Quantitative Biology and Human Behavior, 5812 South Ellis Ave, The University of Chicago, Chicago, IL 60637, USA

Abstract

Functionalization of quantum dots (QDs) with a single biomolecular tag using traditional approaches in bulk solution has met with limited success. DNA polyhedra consist of an internal void bounded by a well-defined three-dimensional structured surface. The void can house cargo and the surface can be functionalized with stoichiometric and spatial precision. Here, we show that monofunctionalized QDs can be achieved by encapsulating QDs inside DNA icosahedra and functionalizing the DNA shell with an endocytic ligand. We deployed the DNA-encapsulated QDs for real time imaging of three different endocytic ligands - folic acid, galectin-3 (Gal3) and the Shiga toxin B-subunit (STxB). Single particle tracking of Gal3 or STxB-functionalized, QD-

[8]Correspondence and requests for materials should be addressed to: ludger.johannes@curie.fr, benoit.dubertret@espci.fr and yamuna@uchicago.edu.

Author contributions

DB and YK conceived the project and designed experiments; DB performed all experiments, some collaboratively, CW, MN, SA, CG, BN, contributed reagents and tools; SA, VP, VC performed key experiments, HJ and PM designed and performed molecular dynamics, DB, CW, PKM, LJ, BD, YK designed experiments and analyzed data, DB, LJ and YK co-wrote the paper. All the authors discussed the results and the paper.

Competing financial interests: BD owns NexDot, a for-profit company that provided some of the quantum dots used in this study.

Additional Information: Reprints and permission information is available online at www.nature.com/reprints.

Europe PMC Funders Author Manuscripts

loaded DNA icosahedra allows us to monitor compartmental dynamics along endocytic pathways. These DNA-encapsulated QDs that bear a unique stoichiometry of endocytic ligands represent a new class of molecular probes for quantitative imaging of endocytic receptor dynamics.

Europe PMC Funders Author Manuscripts

The ubiquitous deployment of quantum dots (QDs) in biology has been constrained due to lack of methodologies to permanently and homogenously monofunctionalize them1. Traditional approaches to achieve this involve coupling QDs and ligands in fixed ratios in solution (Supplementary table 1)2–7. This has met with limited success due to stochastic control over ligand stoichiometry leading to sample heterogeneity.

Structural DNA nanotechnology has yielded diverse, well-defined, nanoscale polyhedra8,9 These polyhedra enclose an internal void that can house nanoscale cargo and possess a well-defined surface for molecular display with both stoichiometric and spatial precision8,10–17. DNA icosahedra can encapsulate cargo without compromising cargo functionality and can be targeted to specific endocytic pathways8,12. Here, we combine the photostability of QDs, with the molecular programmability of the DNA polyhedra by encapsulating QDs inside DNA icosahedra displaying a solitary bio-molecular tag. This is a new class of precisely functionalized particles of homogenous stoichiometry for long duration live imaging.

We first pinpoint specific residues on the icosahedron for optimal surface display of biological tags. We then encapsulate QDs in the icosahedron and monofunctionalize the scaffold with folic acid (FA), galectin-3 (Gal3), or Shiga toxin B-subunit (STxB). The stability of QDs by previous approaches is limited in that ligands on the QD surface are labile and can leach off leading to loss of the tag or QD aggregation18,19. In our approach, this problem is overcome since the issue of QD surface chemistry is completely transferred to the robust, controllable chemistry of DNA. Monofunctionalization is achieved by conjugating the bio-tag to an amine group displayed on the DNA shell without engaging the QD. This effectively results in stably monofunctionalized QDs. Using DNA-encapsulated, QDs monofunctionalized with Gal3 or STxB as endocytic ligands, we track plasma membrane binding, bending, intracellular uptake and long duration dynamics of endocytic carriers on the Gal3/STxB pathways20.

Encapsulation of QDs within DNA icosahedra

CdSe/CdS/ZnS-based quantum dots of 5 nm diameter (QD5) were synthesized as described (Supplementary Fig. S1)21. DNA icosahedra, I, were assembled from three types of five-way junctions (5WJs), V, U and L8. To encapsulate QDs within DNA icosahedra, two half-icosahedra VU_5 and VL_5 were incubated in the presence of excess of QD5 (Fig. 1a and methods). QD-loaded DNA icosahedra were purified by gel electrophoresis and size-exclusion chromatography, (SEC-HPLC; Fig. 1b-c). A size fraction corresponding to the DNA icosahedra showed fluorescence corresponding to QD5, indicating the formation of an I-QD5 complex (I_{QD}) (Supplementary Fig. S2,6). Dynamic light scattering (DLS) studies revealed that free QD5 showed an R_H 4.5±1.8 nm, while I showed an R_H of 9.5±0.1 nm (Fig. 1d, Supplementary Fig. S3). Purified I_{QD} showed an R_H of 10.6±0.4 nm (Fig. 1d). This implies that QD5 in I_{QD} associates with the DNA icosahedron such that it does not

significantly alter the icosahedron dimensions. For an electron dense particle such as QD5 this is possible only if QD5 is encapsulated within the DNA icosahedron.

Since the DNA icosahedron has a pore size of ~2.5 nm8, we used a differential quenching assay to test whether the QDs were encapsulated6. Free QD5 and I_{QD} were subjected to quenchers of sizes ranging from 0.5-5 nm. The fluorescence intensities of 5 nM free QD5 and I_{QD} were measured in the presence of fixed amounts of each quencher. When treated with $1/K_{SV}$ concentrations12 of each quencher, quenchers of all sizes quenched QD5 fluorescence intensity by 50% (Fig. 1e, Supplementary Fig. S4). However, for I_{QD}, only quenchers below ~2.2 nm diameter quenched its fluorescence by 50%. Quenchers ≥3 nm could not quench I_{QD5} fluorescence at all, while quenchers between 2.2-3 nm partially quenched the fluorescence (Fig. 1e). This confirms that QD5 in I_{QD} is physically encapsulated as cargo within the DNA icosahedron. This was reaffirmed by experiments with single QDs or single I_{QD} performed on a confocal microscope22 (Fig. 1f, Supplementary Fig. S5 & S6).

QDs with sizes from 5 to 11 nm, with different surface chemistries, could be encapsulated in DNA icosahedra indicating the generalizability of this method. The capacity of DNA icosahedra to encapsulate nanoparticles was demonstrated by transmission electron microscopy (TEM) where QDs were substituted with 10 nm gold nanoparticles (GNP10) (Fig. 1g, Supplementary Fig. S7). The sizes of the DNA shell were between 15-25 nm, consistent with previous TEM measurements of DNA icosahedra8.

Endocytic uptake maps nucleotide positions on the DNA Icosahedron

To target QD-loaded DNA cages along specific endocytic pathways, we first identified those nucleotide positions on the DNA scaffold where a conjugated molecular tag faces the external milieu. We developed an atomistic model of the DNA icosahedron conjugated to folic acid (FA) using xLeAP module in AMBER and studied its *in silico* stability using molecular dynamics (MD) simulations (see methods)23–26. After 50 ns of simulation, the structure displayed moderate deviations along the edges and minor structural changes at the 5WJs. However, it retained its icosahedral geometry indicating the overall stability of the architecture *in silico* (Fig. 2a-b).

We then conjugated a small endocytic ligand, folic acid (FA) to different nucleotide positions along a given edge of the DNA icosahedron and quantitated FA accessibility by endocytic uptake in cells expressing the folate receptor27. Seven different folate-conjugated icosahedra (I^{FA}) were realized, each with a single folate tag at residues 7, 9, 11, 13, 15, 17, and 19 away from the vertex V, collectively spanning a full helical turn (Supplementary Fig. S8a,b). An Alexa 647 fluorophore was also incorporated on I^{FA} to give $I^{FA/A647}$ in order to visualize the icosahedral shell. IA2.2 cells stably expressing the human transferrin and folate receptors, were pulsed with 100 nM of each of the seven distinct $I^{FA/A647}$ samples along with 100 nM fluorescent transferrin (Tf^{A568}) to normalize for endocytic uptake. $I^{FA/A647}$ samples with FA tags located at positions 11 and 13 showed maximal endocytic uptake that decreased sharply as the position of the tag was moved along either direction (Fig. 2c). This is consistent with the atomistic model where, at positions 11 and 13 the FA tag is maximally

exposed, reaffirming its enhanced accessibility to the folate receptor (Supplementary Fig. S18).

We then tested whether $I^{FA/A647}$ was endocytosed specifically by the folate receptor pathway (Fig. 2d-e). $I^{FA/A647}$ with FA at position 11, hereafter designated as $I^{FA/A647}$, showed efficient uptake and colocalization with endocytic markers Tf (Fig. 2d, upper panels) and pteroyl lysine bodipy-TMR (PLB), a fluorescent analog of folic acid (Fig. 2d, lower panels). When $I^{FA/A647}$ was co-pulsed with 10 fold excess free FA, it was successfully competed out (Fig. 2f, upper panels). I^{A647} without an FA tag also showed no uptake. When IA2.2 cells lacking the folate receptor were pulsed with $I^{FA/A647}$ no uptake was observed (Fig. 2f, lower panels). This indicates that uptake of $I^{FA/A647}$ needs the folate tag and occurs via the folate receptor pathway (Fig. 2f-g). Further, the internalization efficiency showed a sinusoidal pattern as a function of nucleotide position, with a periodicity that matches the pitch of a B-DNA helix (Figure 2c). This proves monofunctionalization of DNA architectures in bulk solution28,29.

Given that monofunctionalized DNA icosahedra mark a specific endocytic route, we combined this with I_{QD} bearing an FA tag at position 11 (I_{QD}^{FA}). I_{QD}^{FA} was efficiently uptaken and colocalized with Tf^{A488} showing specific targeting of I_{QD}^{FA} along the folate pathway (Fig. 2h,i). Thus we could realise molecularly identical I_{QD}s displaying a single ligand on the icosahedral DNA shell accessible to its cognate endocytic receptor.

Binding and endocytic uptake of I_{QD}^{Gal3} and I_{GNP}^{Gal3}

We confirmed monofunctionalization as well as expanded the range of conjugated endocytic tags by probing the stoichiometry of a cellular lectin, galectin-3 (Gal3), conjugated to the DNA icosahedron (Fig. 3a, Supplementary Fig. 9). DNA icosahedra bearing a surface displayed amine group (I^{NH2}) were each loaded with a solitary 10 nm gold nanoparticle (GNP10) to give I_{GNP}^{NH2}, as previously described30. His-tagged Gal3 bearing an engineered cysteine residue (His-Gal3/Cys) was conjugated to I_{GNP}^{NH2} and purified to give $I_{GNP}^{His\text{-}Gal3}$ (Supplementary Fig. S9a,b). To $I_{GNP}^{His\text{-}Gal3}$ deposited on a TEM grid, 5 nm gold nanoparticles bearing Ni-nitrilotriacetate (GNP5) was added. When visualized by TEM, 74% of 10 nm GNPs were present in close proximity with a GNP5 (Fig. 3b-d). We also observed 23% of solitary 10 nm GNPs, probably due to $I_{GNP}^{His\text{-}Gal3}$ orientations on the grid where the Gal3 tag is inaccessible to GNP5. 3% of $I_{GNP}^{His\text{-}Gal3}$ showed more than one proximal GNP5. Indeed, pure GNP5 solutions show ~30% dimers/oligomers, which cannot be abolished even with strong sonication and dilution (Supplementary Fig. S10). Non-functionalized I_{GNP} shows no such paired association with GNP5 (Supplementary Fig S10). Thus, single particle TEM analysis revealed that the robust generation of monofunctionalized, cargo-loaded DNA icosahedra in high yields (65-90%; Fig. 3c).

Given the exquisite control over mono-functionalization, we tested whether I_{QD}^{Gal3} could be applied to transport QDs or GNPs intracellularly and probe the Gal3 endocytic pathway. Gal3 binds glycosylated proteins such as β1 integrin and CD44 that are resident on the plasma membrane of cells. Gal3 then undergoes oligomerization driving biogenesis of morphologically distinct crescent-shaped clathrin-independent carriers (CLICs) mediated by

glycosphingolipids31. CLICs eventually fuse with early/sorting endosomes32. Using sulfo-MBS chemistry, Gal3/Cys was conjugated to I_{QD} to give I_{QD}^{Gal3}. We tested the cellular binding and uptake pathway of I_{QD}^{Gal3} by colocalization with fluorescently labeled Gal3 ($Gal3^{Cy5}$)(Fig. 3e, Supplementary Fig. S9a-c). I_{QD}^{Gal3} and $Gal3^{Cy5}$ bound the plasma membrane of mouse embryonic fibroblasts (MEFs) efficiently with quantitative colocalization (Fig. 3e). In the presence of a specific Gal3 competitor such as lactose (100 mM), binding of both I_{QD}^{Gal3} and $Gal3^{Cy5}$ was reduced by 95% indicating that binding was specific (Fig. 3f). Upon depleting cellular ATP, the scission of Gal3-induced membrane invaginations is inhibited leading to distinctive, long, tubular plasma membrane invaginations31. When I_{QD}^{Gal3} and $Gal3^{Cy5}$ were incubated with ATP-depleted cells on ice for 30 min, both I_{QD}^{Gal3} and $Gal3^{Cy5}$ colocalized in long, tubular plasma membrane invaginations (Fig. 3g). Thus I_{QD}^{Gal3} retains its binding specificity to the cell membrane and induces downstream plasma membrane invagination.

Gal3-induced CLICs are distincitive, crescent-shaped, short, tubular structures as revealed by TEM31. To unequivocally prove that I_{QD}^{Gal3} is internalized by the Gal3 pathway, we sought to visualize I^{Gal3} within such CLICs. To facilitate visualization by TEM, we created I_{GNP}^{Gal3}, encapsulating 5-6 GNPs of ~5 nm diameter30. MEFs were incubated with Gal3 conjugated to horseradish peroxidase (Gal3-HRP) and I_{GNP}^{Gal3} in a 1:1 ratio and HRP was developed using 3,3'-diaminobenzidine-H_2O_2. TEM (see methods) images of these cells clearly revealed crescent shaped structures near the plasma membrane - the definitive signature of CLICs (Fig. 4a-c). Under low contrast conditions, CLICs containing clusters of 5 nm GNPs could clearly be seen, indicating that I_{GNP}^{Gal3} and Gal3-HRP are endocytosed together into CLICs (Fig. 4b-c, right panels). From two independent experiments, comprising 25 cells, 94% of GNPs localized in DAB precipitate-positive structures (Fig. 4b,c), confirming that I_{GNP}^{Gal3} adopts the same pathway as Gal3. Consistent with literature, 78% of the intracellular structures had CLIC morphology31.

To address the endocytic fate of these particles, I_{QD}^{Gal3} and Gal3-Cy5 were co-incubated with MEFs for 2, 15 and 60 min (Fig. 4d, Supplementary fig. S15). At 2 min, I_{QD}^{Gal3} and Gal3-Cy5 colocalized in small vesicular structures close to the plasma membrane (Fig. 4d, upper panel). At 15 min, they colocalized in larger punctate structures, likely corresponding to early/sorting endosomes31 (Fig. 4d, middle panel). At 60 min, I_{QD}^{Gal3} and Gal3-Cy5 colocalized in large, ring-like, perinuclear structures, likely corresponding to late endosomes (Fig. 4d, lower panel). This quantitative colocalization with Gal3-Cy5 along the entire pathway (Pearson's coefficient > 0.8, Spearman's coefficient > 0.9 and Mander's coefficient > 0.9 at all time points), confirmed that post attachment of Gal3, I_{QD} does not alter Gal3 internalization characteristics.

Single molecule tracking of I_{QD}^{STxB} uptake in live cells

The B-subunit of Shiga toxin (STxB) is a homopentameric protein that binds the glycosphingolipid Gb3 on the plasma membrane of particular eukaryotic cells. Post binding, STxB pentamers cluster to drive the formation of membrane invaginations that undergo dynamin, endophilin-A2 and actin-dependent scission to form endocytic carriers that then fuse with early endosomes33–35, followed by further trafficking along the retrograde

route36. An STxB variant carrying an engineered cysteine residue at its C-terminal end was coupled to monofunctionalized I_{QD}s, as described earlier (Supplementary figs S11-13) to give I_{QD}^{STxB}. Alexa488 labeled STxB ($STxB^{A488}$) and I_{QD}^{STxB} efficiently bound the plasma membrane, were internalized into punctate structures and colocalized with each other (Fig. 5a,b). Further, I_{QD}^{STxB} localized in early endosomes (EE) via the STxB internalization pathway (Supplementary Fig. S14 & S17).

Given the specific uptake of I_{QD}^{STxB} and photostability of QDs, we investigated the dynamics of STxB-mediated endocytic transport by real-time TIRF microscopy, with single particle precision (Supplementary Fig. S16). HeLa cells were pulsed with a mixture of ~200 nM unlabelled STxB doped with 50 pM I_{QD}^{STxB}. This induced efficient clustering of STxB on the membrane that incorporated I_{QD}^{STxB} within larger STxB clusters. Upon internalisation, I_{QD}^{STxB} disappeared from the plasma membrane plane of observation (Fig. 5c, left panel, Supplementary movie S1). Before internalization, most I_{QD}^{STxB} particles undergo hop diffusion characterized by motion in confined spaces followed by sudden jumps (Fig.5c, middle and right panels, Supplementary movie S2). I_{QD}^{STxB} diffusion on the extracellular leaflet of the plasma membrane therefore follows a complex diffusion behaviour that suggests picket-fence type compartmentalization by the underlying actin meshwork, as seen in phospholipids37. Compartment sizes characterized by the confined diffusion ranged from 30-80 nm with average diffusion coefficients of 0.12 $\mu m^2/s$, similar to those observed for transferrin receptors38.

Endosomes containing I_{QD}^{STxB} colocalized with and moved along microtubules actively, (Fig. 5d, Supplementary movie S3), transferring back and forth between microtubules (Supplementary movie S4). Endosomes showed bursts of active transport with pause intervals indicating either normal or confined diffusive behaviour respectively (Fig. 5e). A single endosome switches between these two modes, with active bursts showing run lengths of 2.4 ± 1.4 μm and average speeds of 0.5 ± 0.2 μm/s. We used mean square displacement analysis (MSD) from where α values were used to characterize the spectrum of motion observed for a population of endosomes. A measure of the scaling exponent, $\alpha < 0.4$ indicates confined motion, $0.4 < \alpha < 1.45$ indicates diffusive motion, while $\alpha > 1.45$ indicates directed motion. The observed distribution of α values in our data (see SI, methods) reveals that a majority of endosomes, at any given time display either confined or diffusive behaviour (Fig. 5e). This average value is similar to velocities observed in previous studies of Rab5 positive endosomes, suggesting that most of the motile I_{QD}^{STxB} observed are in early endosomes39. Stochastic active bursts result in the overall transport of endosomes. The active motions also showed reversals, suggesting that both plus and minus end microtubule-associated motors are present on the endosomes. The observed pauses may arise from several phenomena: endosomes crossing over at intersections of microtubules, interaction with ER, actin meshwork or other organelles40,41. Endosomes containing I_{QD}^{STxB} could be categorized into static early endosomes (SEE) and dynamic endosomes (DE), as observed previously for transmembrane cargo and viral particles42. Internalized I_{QD}^{STxB} actively moved and fused with SEE (Fig. 5f, yellow arrows). Small vesicles containing I_{QD}^{STxB} emerge from these SEE and then move actively, constituting dynamic endosomes (DE) (Fig. 5f, white arrows). The broad range of α values reflects the crowded nature of the intracellular milieu and the interaction of I_{QD}^{STxB} containing endosomes with

various intracellular structures such as actin meshwork or the microtubule network in between directed active runs39.

Conclusions

We show the efficient encapsulation of quantum dots (QDs) within a DNA icosahedron in bulk solution. Encapsulation does not alter QD fluorescence properties *in vitro* or in the cellular milieu. Endocytic uptake assays supported by molecular modeling studies pinpointed residues on the icosahedron that display biological tags most efficiently. By site-specifically monofunctionalizing these icosahedra with endocytic tags we could realize QDs homogenously bearing a single targeting ligand (folate/Gal3/STxB). This enabled the live tracking of long duration compartment dynamics in cells. This methodology is generalizable across both QDs and endocytic tags, due to the capsular DNA interface. As the icosahedral DNA surface is well defined, one can envisage homogenous oligofunctionalization of I_{QD}s with ligands. These could probe receptor-ligand interactions and oligomerization, whose nature and consequences change with ligand-receptor stoichiometries.

Methods

Materials

The unlabeled and modified, labeled oligonucleotides (HPLC-purified and lyophilized) were obtained from IBA GmbH. N-cyano imidazole (NCI) was synthesized in-house according to previous protocols30. 1-octadecene (ODE, Sigma), oleylamine (Sigma), oleic acid (Sigma), trioctylphosphine (TOP, Cytec), cadmium oxide (Sigma), selenium pellets (Sigma), sulfur powder (Sigma) and tetradecylphosphonic acid (TDPA, PCI synthesis) were purchased from the indicated suppliers. Methods for DNA icosahedron construction and characterization have been previously described30. CdSe/CdS/ZnS QDs were synthesized according to previously published protocols21. The detailed procedures for synthesis, characterization and encapsulation of QDs within DNA icosahedron are provided in the supplementary information. The experiments on cells were carried out using QDs provided by Nexdot (www.nexdot.fr).

Cell Culture and labeling with endocytic markers

IA2.2 cell line is a Chinese hamster ovary (CHO) cell line that lacks endogenous transferrin receptors but stably expresses the human transferrin and folate receptors described in reference 43. The cells were cultured in Ham's-F12 Complete media (HF-12, Himedia) containing 10% heat-inactivated FBS, 100 μg/mL streptomycin and 100 μg/mL penicillin with 200 μg/mL G418 and 100 μg/mL hygromycin to ensure maintenance of the transferrin and folate receptors. HeLa (source described in reference 44), Rab5-GFP expressing HeLa cells and MEFs cells (source described in ref 31) were cultured in DMEM media supplemented with 10% FCS and PS mixture. For binding experiments, IA2.2 cells were pulsed for 30 min on ice with 100 nM concentrations of all probes (I_{QD}^{FA}, Tf or PLB), washed 2-3 times with M1 media, and imaged under Olympus FV1000 confocal microscope, using appropriate lasers and imaging conditions. For the uptake assay, cells were pulsed for 15 min at 37°C with the indicated probes, washed and imaged. Uptake and

colocalization were quantified using the Pearson colocalization coefficient application in ImageJ (NIH). His-tagged cysteine engineered Gal3 was purified according to previously established protocol34. Cysteine engineered Gal3 and STxB were conjugated to amine modified DNA using sulfo-MBS or SM(PEG)8 (PierceNet) crosslinkers. Labeled Gal3/STxB and DNA-Gal3/DNA-STxB were pulsed to cells at 50 or 100 nM concentrations in DMEM media for the indicated periods of time. Post incubation cells were washed with PBS, fixed in 4% PFA, and coverslips mounted on fluoromount Mowiol for imaging. For fixed samples, imaging was performed using a Leica epifluorescence microscope, and for live cell and single particle tracking, A1R confocal, TIRF-FRAP and spinning disk SP7 microscopes from Nikon were used. The detailed procedures are provided in supplementary information.

Supplementary Material

Refer to Web version on PubMed Central for supplementary material.

Acknowledgements

The authors thank Sunaina Surana and Thomas Pons for discussions and suggestions. The imaging facilities CIFF at NCBS and PICT-IBiSA / Nikon Imaging Centre at *Institut Curie*-CNRS and the France-BioImaging infrastructure (ANR-10-INSB-04) are acknowledged. DB thanks CEFIPRA for the Charpak fellowship, Institute Curie and HFSP for postdoctoral fellowships. This work was supported by the following grants 4803-B from CEFIPRA to BD and YK, RGP0029-2014 from HFSP to YK and LJ, Agence Nationale pour la Recherche ANR-09-BLAN-283 from FPGG, to BD and LJ, ANR-11 BSV2 014 03 to LJ, project 340485 from the European Research Council to LJ, UL1 TR000430 from National Center for Advancing Translational Sciences of the NIH and startup support from University of Chicago to YK. The Johannes team is members of *Labex CelTisPhyBio* (11-LBX-0038) and of *Idex Paris Sciences et Lettres* (ANR-10-IDEX-0001-02 PSL).

References

1. Kairdolf, Ba, et al. Semiconductor quantum dots for bioimaging and biodiagnostic applications. Annu Rev Anal Chem. 2013; 6:143–162.
2. You C, et al. Self-controlled monofunctionalization of quantum dots for multiplexed protein tracking in live cells. Angew Chemie - Int Ed. 2010; 49:4108–4112.
3. Clarke S, et al. Covalent monofunctionalization of peptide-coated quantum dots for single-molecule assays. Nano Lett. 2010; 10:2147–2154. [PubMed: 20433164]
4. You C, et al. Electrostatically controlled quantum dot monofunctionalization for interrogating the dynamics of protein complexes in living cells. ACS Chem Biol. 2013; 8:320–326. [PubMed: 23186299]
5. Carstairs HMJ, Lymperopoulos K, Kapanidis AN, Bath J, Turberfield AJ. DNA monofunctionalization of quantum dots. ChemBioChem. 2009; 10:1781–1783. [PubMed: 19554595]
6. Howarth M, et al. Monovalent, reduced-size quantum dots for imaging receptors on living cells. Nat Methods. 2008; 5:397–399. [PubMed: 18425138]
7. Farlow J, et al. Formation of targeted monovalent quantum dots by steric exclusion. Nat Methods. 2013; 10:1203–5. [PubMed: 24122039]
8. Bhatia D, et al. Icosahedral DNA nanocapsules by modular assembly. Angew Chemie - Int Ed. 2009; 48:4134–4137.
9. Pan K, et al. Lattice-free prediction of three-dimensional structure of programmed DNA assemblies. Nat Commun. 2014; 5:5578. [PubMed: 25470497]
10. Zhang C, et al. Exterior modification of a DNA tetrahedron. Chem Commun (Camb). 2010; 46:6792–6794. [PubMed: 20730149]

11. Angell C, Xie S, Zhang L, Chen Y. DNA Nanotechnology for Precise Control over Drug Delivery and Gene Therapy. Small. 2016; :1–16. DOI: 10.1002/smll.201502167
12. Bhatia D, Surana S, Chakraborty S, Koushika SP, Krishnan YA. synthetic icosahedral DNA-based host-cargo complex for functional in vivo imaging. Nat Commun. 2011; 2:339. [PubMed: 21654639]
13. Surana S, Bhatia D, Krishnan Y. A method to study in vivo stability of DNA nanostructures. Methods. 2013; 64:94–100. [PubMed: 23623822]
14. Edwardson TGW, Carneiro KMM, McLaughlin CK, Serpell CJ, Sleiman HF. Site-specific positioning of dendritic alkyl chains on DNA cages enables their geometry-dependent self-assembly. Nat Chem. 2013; 5:868–75. [PubMed: 24056344]
15. McLaughlin CK, et al. Three-dimensional organization of block copolymers on 'DNA- minimal' scaffolds. J Am Chem Soc. 2012; 134:4280–4286. [PubMed: 22309245]
16. Perrault SD, Shih WM. Virus-inspired membrane encapsulation of DNA nanostructures to achieve in vivo stability. ACS Nano. 2014; 8:5132–5140. [PubMed: 24694301]
17. Lee H, et al. Molecularly self-assembled nucleic acid nanoparticles for targeted in vivo siRNA delivery. Nat Nanotechnol. 2012; 7:389–93. [PubMed: 22659608]
18. Jaiswal JK, Simon SM. Imaging single events at the cell membrane. Nat Chem Biol. 2007; 3:92–98. [PubMed: 17235347]
19. Alivisatos, aP; Gu, W.; Larabell, C. Quantum dots as cellular probes. Annu Rev Biomed Eng. 2005; 7:55–76. [PubMed: 16004566]
20. Johannes L, Parton RG, Bassereau P, Mayor S. Building endocytic pits without clathrin. Nat Rev Mol Cell Biol. 2015; 42:1–11.
21. Carion O, Mahler B, Pons T, Dubertret B. Synthesis, encapsulation, purification and coupling of single quantum dots in phospholipid micelles for their use in cellular and in vivo imaging. Nat Protoc. 2007; 2:2383–2390. [PubMed: 17947980]
22. Mahler B, et al. Towards non-blinking colloidal quantum dots. Nat Mater. 2008; 7:659–664. [PubMed: 18568030]
23. Cornell WD, et al. A second generation force field for the simulation of proteins, nucleic acids, and organic molecules. J Am Chem Soc. 1995; 117:5179–5197.
24. Santosh M, Maiti PK. Structural rigidity of paranemic crossover and juxtapose DNA nanostructures. Biophys J. 2011; 101:1393–1402. [PubMed: 21943420]
25. Joshi H, Dwaraknath A, Maiti PK. Structure, stability and elasticity of DNA nanotubes. Phys Chem Chem Phys. 2014; 17:1424–1434. [PubMed: 25427873]
26. Maiti PK, Pascal Ta, Vaidehi N, Heo J, Goddard Wa. Atomic-level simulations of seeman DNA nanostructures: the paranemic crossover in salt solution. Biophys J. 2006; 90:1463–1479. [PubMed: 16478709]
27. Sabharanjak S, Mayor S. Folate receptor endocytosis and trafficking. Adv Drug Deliv Rev. 2004; 56:1099–1109. [PubMed: 15094209]
28. Furey WS, et al. Use of fluorescence resonance energy transfer to investigate the conformation of DNA substrates bound to the Klenow fragment. Biochemistry. 1998; 37:2979–2990. [PubMed: 9485450]
29. Erben CM, Goodman RP, Turberfield AJ. Single-molecule protein encapsulation in a rigid DNA cage. Angew Chemie - Int Ed. 2006; 45:7414–7417.
30. Bhatia D, Chakraborty S, Mehtab S, Krishnan Y. A method to encapsulate molecular cargo within DNA icosahedra. Methods Mol Biol. 2013; 991:65–80. [PubMed: 23546660]
31. Lakshminarayan R, et al. Galectin-3 drives glycosphingolipid-dependent biogenesis of clathrin-independent carriers. Nat Cell Biol. 2014; 16:595–606. [PubMed: 24837829]
32. Delacour D, et al. Apical sorting by galectin-3-dependent glycoprotein clustering. Traffic. 2007; 8:379–388. [PubMed: 17319896]
33. Römer W, et al. Shiga toxin induces tubular membrane invaginations for its uptake into cells. Nature. 2007; 450:670–675. [PubMed: 18046403]
34. Römer W, et al. Actin Dynamics Drive Membrane Reorganization and Scission in Clathrin-Independent Endocytosis. Cell. 2010; 140:540–553. [PubMed: 20178746]

35. Renard H-F. Endophilin-A2 functions in membrane scission in clathrin-independent endocytosis. Nature. 2015; 517:493–6. [PubMed: 25517096]
36. Johannes L, Popoff V. Tracing the Retrograde Route in Protein Trafficking. Cell. 2008; 135:1175–1187. [PubMed: 19109890]
37. Kusumi A, Ike H, Nakada C, Murase K, Fujiwara T. Single-molecule tracking of membrane molecules: Plasma membrane compartmentalization and dynamic assembly of raft-philic signaling molecules. Semin Immunol. 2005; 17:3–21. [PubMed: 15582485]
38. Kusumi, a; Sako, Y.; Yamamoto, M. Confined lateral diffusion of membrane receptors as studied by single particle tracking (nanovid microscopy). Effects of calcium-induced differentiation in cultured epithelial cells. Biophys J. 1993; 65:2021–2040. [PubMed: 8298032]
39. Wang B, Kuo J, Granick S. Bursts of active transport in living cells. Phys Rev Lett. 2013; 111:1–16.
40. Bálint Š S, Verdeny Vilanova I, Sandoval Álvarez Á, Lakadamyali M. Correlative live-cell and superresolution microscopy reveals cargo transport dynamics at microtubule intersections. Proc Natl Acad Sci U S A. 2013; 110:3375–80. [PubMed: 23401534]
41. Zajac AL, Goldman YE, Holzbaur ELF, Ostap EM. Local cytoskeletal and organelle interactions impact molecular-motor-driven early endosomal trafficking. Curr Biol. 2013; 23:1173–1180. [PubMed: 23770188]
42. Lakadamyali M, Rust MJ, Zhuang X. Ligands for clathrin-mediated endocytosis are differentially sorted into distinct populations of early endosomes. Cell. 2006; 124:997–1009. [PubMed: 16530046]
43. Mayor S, Maxfield FR. Insolubility and redistribution of GPI-anchored proteins at the cell surface after detergent treatment. Mol Biol Cell. 1995; 6:929–44. [PubMed: 7579703]
44. Römer W, et al. Shiga toxin induces tubular membrane invaginations for its uptake into cells. Nature. 2007; 450:670–675. [PubMed: 18046403]

Europe PMC Funders Author Manuscripts

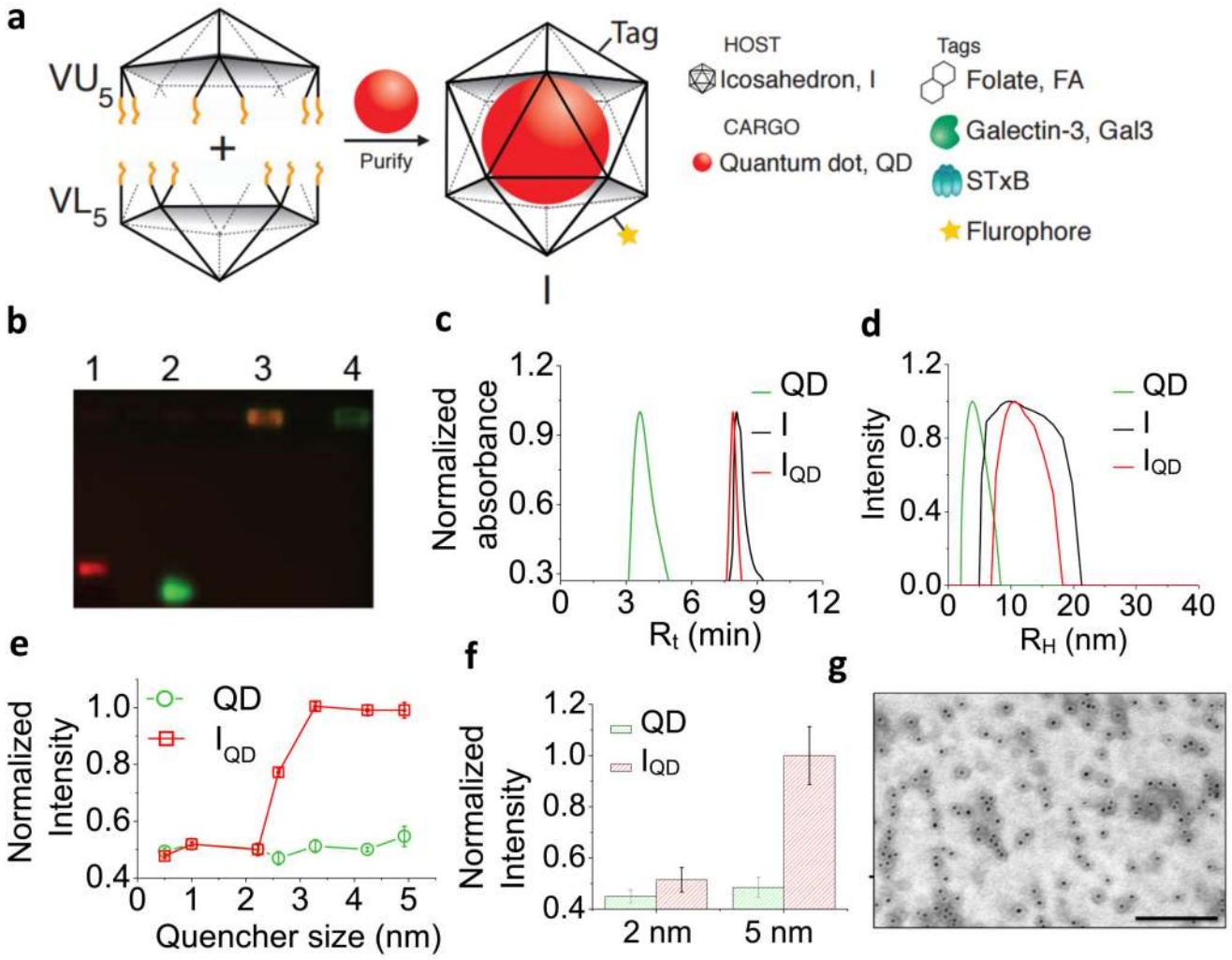

Fig. 1. Encapsulation of quantum dots (QDs) within DNA icosahedra (I).

a, (left) Schematic showing the formation of quantum dot-loaded icosahedra (I_{QD}). Two complementary half icosahedra VU_5/VL_5 are mixed in a 1:1 ratio in the presence of excess QDs, purified from free QDs to get I_{QD}. (right) Cartoon representation of all molecular tags used to functionalize the DNA icosahedron. **b,** Gel electrophoretic mobility shift assay for the formation of I_{QD}. Fluorescence image of 0.8% agarose gel in 1X TAE (λ_{ex} at 488 nm): Lane 1, QD (λ_{em}= 605 nm); lane 2, VU_5^{FITC}(λ_{em}= 520 nm), lane 3, I_{QD}^{FITC}(λ_{em}= 520 & 605 nm), lane 4, I^{FITC} (λ_{em}= 520 nm). **c,** Size-exclusion chromatogram of I_{QD} (red trace) post-gel excision where absorbance at 260 nm was followed. **d,** Dynamic light scattering traces of free QD (green), I (black) and I_{QD} (red). **e,** Fluorescence intensity-based quenching assay for free QD (green) and I_{QD} (red) in bulk solution. Quenchers are gold nanoparticles (GNPs) of indicated sizes, iodide (0.5 nm), TEMPO (1 nm) and TEMPO Dextran (2.5 nm). Mean values of two experiments are presented with corresponding s.d. (n=2). **f,** Single molecule quenching assay for free QD and I_{QD} when subjected to 2 nm and 5 nm size GNPs. Error bars indicate mean of two experiments with associated s.d. (two-tailed unpaired

t-test. * $p < 0.0001$, n=2). **g,** Representative TEM image of GNP-encapsulated DNA icosahedra stained with 1% uranyl acetate. Scale bar: 200 nm.

Europe PMC Funders Author Manuscripts

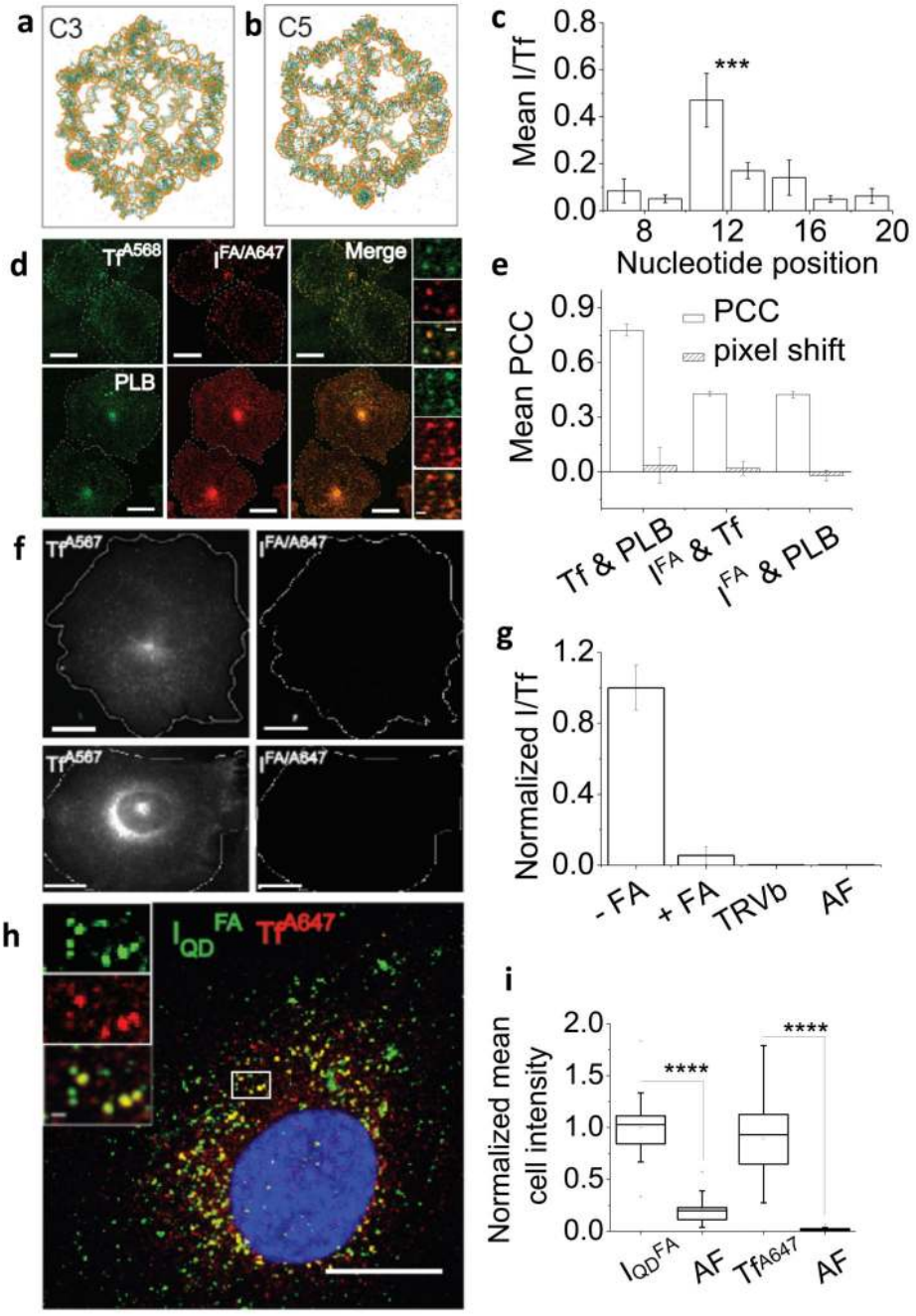

Fig. 2. Cellular validation of atomistic model of DNA icosahedron.

a-b, Atomistic model of charge neutralized, solvent stabilized DNA icosahedron post 50 ns of MD simulation showing **a,** the C3 and **b,** the C5 axes of symmetry. **c,** Cellular uptake of $I^{FA/A647}$ as a function of different nucleotide positions of FA on $I^{FA/A647}$. Uptake is normalized with respect to Tf^{A568} as an internal control. Mean values of total cell intensity from three independent experiments. **d-g,** Uptake of $I^{FA/A647}$ is through the folate receptor pathway. **d,** Colocalization of endosomes containing $I^{FA/A647}$ (red) uptaken by IA2.2 cells with endocytic probes (green) transferrin (Tf^{A568}) and pteroyllysine (PLB). **e,** Quantification

of colocalization of $I^{FA/A647}$ with Tf^{A568} and PLB. Mean Pearson's correlation coefficient (PCC) for n = 20 cells with associated s.d. (n=2) and for images shifted by 10 pixels. **f**, $I^{FA/A647}$ uptake occurs through the FA tag and the folate receptor. $I^{FA/A647}$ uptake in the presence of 10-fold excess FA (upper panels). $I^{FA/A647}$ uptake in TRVb-2 cells lacking the folate receptor (bottom panels). **g**, Quantification of $I^{FA/A647}$ uptake in **f**. Mean values of two independent experiments with associated s.d. **h,i,** QDs encapsulated in I^{FA} ($I_{QD}{}^{FA}$) shows the same uptake pathway as $I^{FA/A647}$. **h,** Cellular uptake of Tf^{A647} (red) and $I_{QD}{}^{FA}$ (green) in IA2.2 cells post 15 min incubation at 37°C. **i,** Endocytic uptake of Tf^{A647} and $I_{QD}{}^{FA}$ quantified for 15 cells. AF = autofluorescence**.** All scale bars are 10 μm, inset scale bars are 5 μm. All error bars are standard errors and use the two-tailed unpaired t-test.

Europe PMC Funders Author Manuscripts

Europe PMC Funders Author Manuscripts

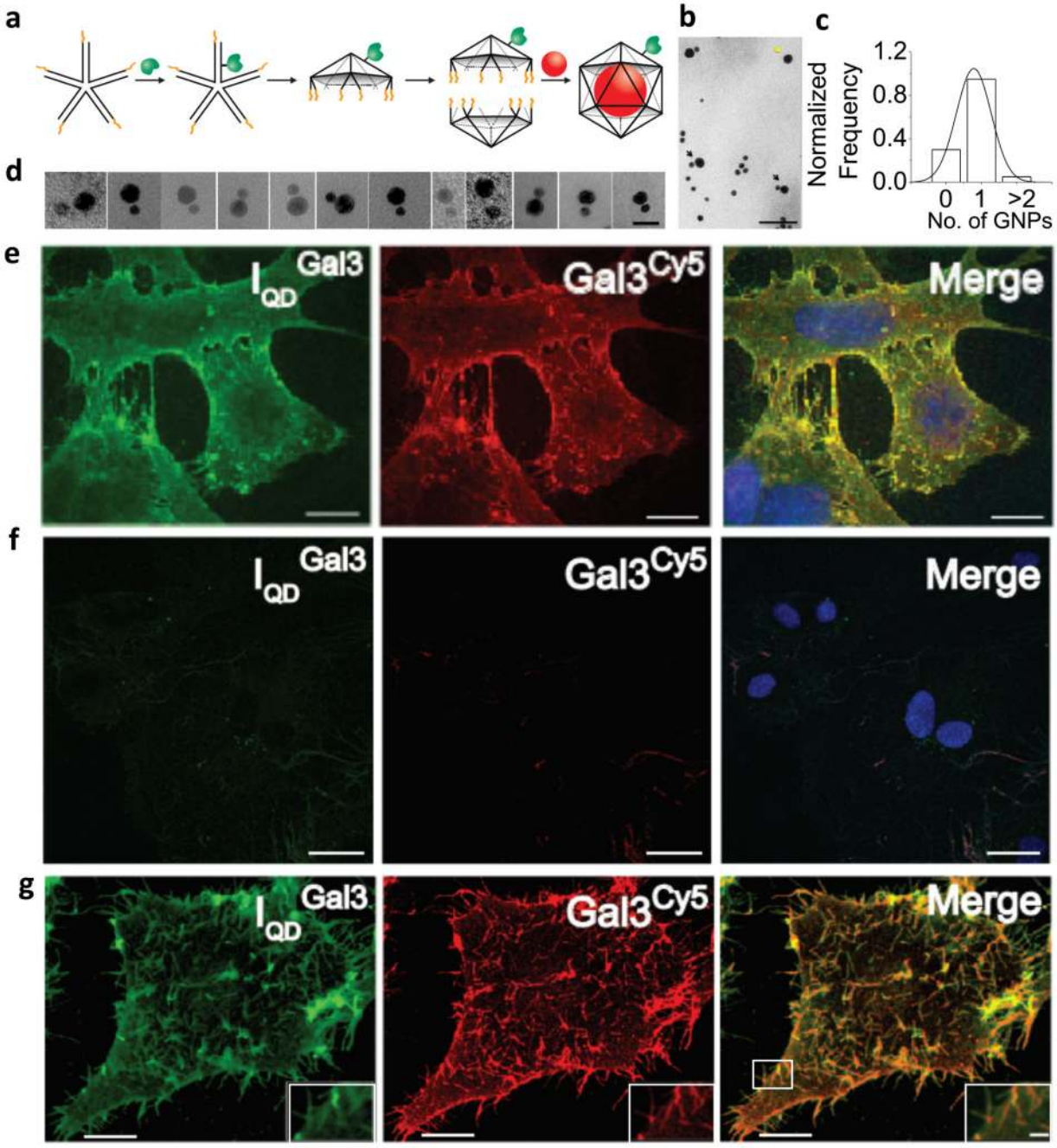

Fig. 3. Binding of I_{QD}^{Gal3} to the plasma membrane of cells:

a. Schematic of the assembly strategy to tag I_{QD} with galectin-3 (Gal3) to give I_{QD}^{Gal3}. U is conjugated to Gal3 and then incorporated into VU_5 to give VU_5^{Gal3}. Assembly of VU_5^{Gal3}, VL_5 and QDs yields I_{QD}^{Gal3}. **b,** TEM images showing that DNA icosahedra each encasing a single 10 nm gold nanoparticle (GNP) is functionalized with a single Gal3 tag. $I_{GNP}^{His\text{-}Gal3}$ incubated with excess of 5 nm NTA-coated GNPs (GNP5) imaged by TEM. Scale bar: 50 nm. **c,** Frequency of the number of GNP5 particles within a 10 nm radius of $I_{GNP}^{His\text{-}Gal3}$ particles **d,** Zoomed images of representative examples of $I_{GNP}^{His\text{-}Gal3}$ attached to a single

GNP5. **e,f.** I_{QD}^{Gal3} and Gal3 show similar plasma membrane binding characteristics. **e**, Fluorescence images of mouse embryonic fibroblasts (MEFs) incubated at 4°C with I_{QD}^{Gal3} (green) and $Gal3^{Cy5}$ (red) **f**, Binding of both I_{QD}^{Gal3} and Gal3 is competed out by 100 mM lactose. **g,** Fluorescence images of I_{QD}^{Gal3} (green) and $Gal3^{Cy5}$ (red) on ATP-depleted MEFs. Insets show tubular membrane invaginations induced by Gal3 due to ATP-depletion. All scale bars: 10 μm. All inset scale bars: 1 μm

Europe PMC Funders Author Manuscripts

Europe PMC Funders Author Manuscripts

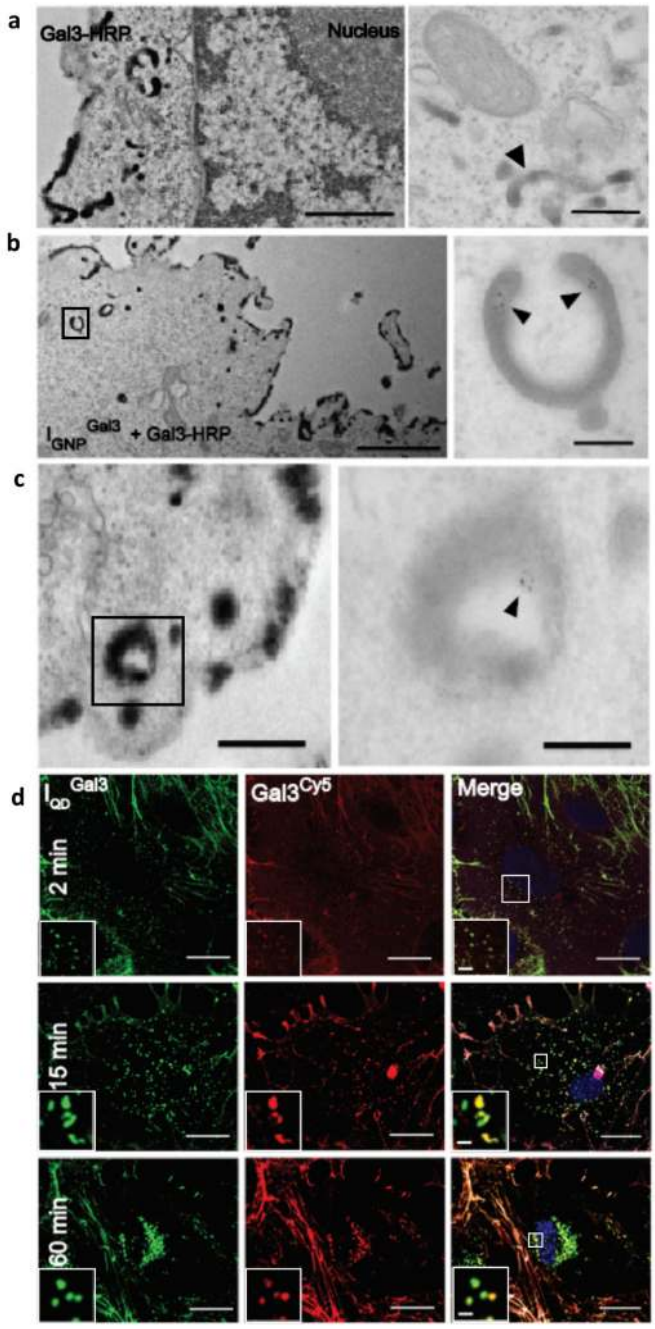

Fig. 4. TEM studies reveal that I_{QD}^{Gal3} is endocytosed through clathrin-independent carriers (CLICs).

a-c, I_{GNP}^{Gal3} is present in CLICs. **a,** TEM sections of MEFs pulsed with Gal3-HRP for 3 min at 37°C and developed with diaminobenzidine/H_2O_2 (left panel). Zoomed image of a Gal3 containing CLIC, showing crescent shaped morphology (see arrowhead, right panel). **b-c** Left panels show representative TEM sections of MEFs pulsed with 1:1 Gal3-HRP : I_{GNP}^{Gal3} at high contrast showing crescent-shaped CLICs (boxed areas) Scale bar: 1 μm. Right panels show zoomed TEM images of boxed regions in the left panels at low contrast

revealing GNPs in the CLICs (arrowheads). Scale bar: 100 nm. **d-f.** I_{QD}^{Gal3} follows the Gal3 endocytic route. **d,** Colocalization of I_{QD}^{Gal3} (green) and $Gal3^{Cy5}$ (red) at the indicated chase times in MEFs: **d**, 2 min in CLICs, **e**, 15 min in early endosomes **f**, 60 min in late endosomes. Scale bar: 10 μm; inset scale bar: 1 μm.

Europe PMC Funders Author Manuscripts

Europe PMC Funders Author Manuscripts

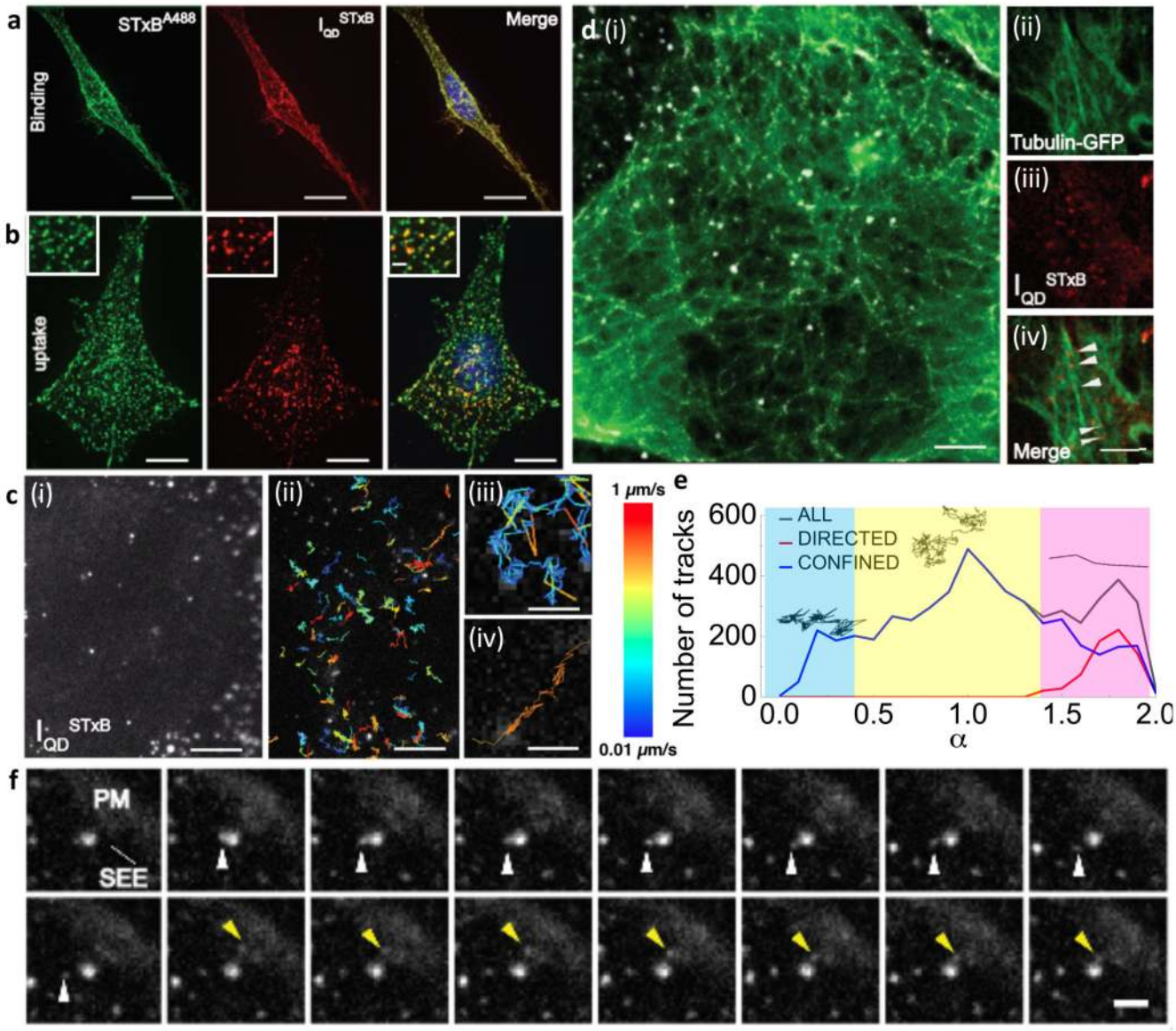

Fig. 5. Single particle tracking of I_{QD}^{STxB} in live cells.

a-b, I_{QD}^{STxB} adopts the STxB endocytic route. **a**, $STxB^{A488}$ (green) and I_{QD}^{STxB} (red) bind the plasma membrane of HeLa cells. **b,** $STxB^{A488}$ (green) and I_{QD}^{STxB} (red) colocalize at 2 min chase time. Inset shows zoomed image of the labelled compartments. **c,** Single particle tracking of I_{QD}^{STxB} bound on the plasma membrane of HeLa cells observed using total internal reflection fluorescence (TIRF) microscopy (see Supplementary movie S1)**.** (i) TIRF image of individual I_{QD}^{STxB} particles bound on the section of the plasma membrane. (ii) A collection of single particle tracks of individual I_{QD}^{STxB} particles, differently colored for clarity, obtained from the region shown in (i) (Supplementary movie S2). (iii-iv) Two typical single particle tracks showing (iii) confined diffusion and (iv) a directed run, both color coded for increasing velocities in μm/s. **d-e,** Single particle tracking of early endosomes containing I_{QD}^{STxB} moving along microtubules in HeLa cells. **d**(i) Spinning disc confocal image of early endosomes containing I_{QD}^{STxB} (white) in HeLa cells expressing tubulin-GFP

(green) (Supplementary movie S3). (ii) Confocal image of early endosomes labeled with I_{QD}^{STxB} (red) localized on microtubules (green), indicated by arrowheads in the merged image. **e,** A plot of frequency of alpha values (α) obtained from ~ 5470 tracks (grey trace). Also shown are the frequency of trajectories showing confined/diffusive behavior (blue trace) and active directed runs (red). The graph is divided into three sections: light blue, yellow and light pink for confined behaviour, diffusive behaviour, and directed runs respectively. Shown on top are typical tracks for each type of behaviour. **f,** Montage of a typical I_{QD}^{STxB} labeled static early endosome or sorting endosome (SEE). The white arrowhead indicates a fission event that gives rise to a smaller dynamic endosome (DE). The yellow arrowhead indicates a fusion event of a vesicle arising from the plasma membrane (PM) with the SEE. All scale bars are: 10 μm. Insets, c(iii), c(iv), d(i) and f scale bars: 1 μm.

Europe PMC Funders Author Manuscripts